





H I Absorption in Low-power Radio AGNs Detected by FAST

Qingzheng Yu (余清正) ¹, Taotao Fang (方陶陶) ¹, Junfeng Wang (王俊峰) ¹ and Jianfeng Wu (武剑锋) ¹

¹Department of Astronomy, Xiamen University, Xiamen, Fujian 361005, People's Republic of China; fangt@xmu.edu.cn, yuqingzheng@stu.xmu.edu.cn

(Received November 19, 2022; Revised May 30, 2023; Accepted June 1, 2023; Published July 25, 2023)

Abstract

We report the discovery of three H I absorbers toward low-power radio active galactic nuclei (AGNs) in a pilot H I absorption survey with the Five-hundred-meter Aperture Spherical radio Telescope (FAST). Compared to past studies, FAST observations have explored lower radio powers by ~ 0.4 dex and detected these weakest absorbers at given redshifts. By comparing the gas properties and kinematics of sources along radio powers, we aim to explore the interplay between AGN and the surrounding interstellar medium (ISM). Compared to brighter sources at similar redshifts, our observations suggest a slightly lower detection rate of H I absorption lines ($\sim 11.5\%$) in low-power radio AGNs with $\log(P_{1.4\text{ GHz}}/W\text{ Hz}^{-1}) = 21.8 - 23.7$. The low-power sources with $\log(P_{1.4\text{ GHz}}/W\text{ Hz}^{-1}) < 23$ have a lower detection rate of $\sim 6.7\%$. Due to the incompleteness of the sample, these detection rates may represent the lower limits. The selection of more extended sources and dilution by H I emission at lower redshifts may contribute to the lower detection rate of H I absorption lines. These detected absorbers present relatively narrow line widths and comparable column densities consistent with previous observations. One absorber has a symmetric profile with a large velocity offset, while the other two show asymmetric profiles that can be decomposed into multiple components, suggesting various possibilities of gas origins and kinematics. These H I absorbers may have connections with rotating disks, gas outflows, galactic gas clouds, gas fueling of the AGN, and jet-ISM interactions, which will be further investigated with the upcoming systematic survey and spatially resolved observations.

Unified Astronomy Thesaurus concepts: Active galactic nuclei (16); Radio spectroscopy (1359); Neutral hydrogen clouds (1099);

1. Introduction

The associated H I 21 cm absorption provides an important method to study the physical conditions of active galactic nuclei (AGNs) and their interplay with the interstellar medium (ISM) of host galaxies (for a review see Morganti & Oosterloo 2018). Previous observations of H I absorption lines in radio AGNs show that the H I gas can be traced in regularly rotating large-scale disks or circumnuclear disks (Gallimore et al. 1999; Struve & Conway 2010; Morganti et al. 2011). Kinematics of the H I absorption lines also have been used to reveal infalling clouds correlated to the feeding of the supermassive black hole (SMBH) (Morganti et al. 2009; Maccagni et al. 2014; Tremblay et al. 2016), as well as outflows or galactic gas clouds indicating the interactions between jets and surrounding ISM (Conway 1999; Morganti et al. 2013; Aditya & Kanekar 2018; Schulz et al. 2021). Observations of H I absorption lines in different types of AGNs can provide

information on the evolution of AGNs and host galaxies, e.g., some recent studies suggest the H I absorption is tightly correlated to galaxy mergers (Dutta et al. 2018, 2019; Dutta & Srikanth 2022).

Although H I absorption has been studied for decades and more than 100 H I absorbers have been detected at $z < 1$ (Morganti & Oosterloo 2018), our understanding is still limited on the H I absorption and related evolution processes in various classes of AGN, especially the faint low-power radio AGNs. Due to the sensitivity limits, most H I 21 cm absorption surveys are limited to bright sources with $S_{1.4\text{ GHz}} > 50$ mJy (Gallimore et al. 1999; Geréb et al. 2015; Aditya 2019). A recent survey carried out with the Westerbork Synthesis Radio Telescope (WSRT) has expanded the sample to weaker sources with $S_{1.4\text{ GHz}} > 30$ mJy (Maccagni et al. 2017) in the redshift range $0.02 < z < 0.25$, which increases detections of H I absorption in low-power radio AGNs ($\log(P_{1.4\text{ GHz}}/W\text{ Hz}^{-1}) < 24$). This survey has found a detection rate of $\sim 27\%$ in the entire sample, and the de-

Corresponding author: Taotao Fang

tection rate remains similar across the range of radio powers. Their results indicate AGNs at the low-power range mostly show narrow absorption features, which traced gas in rotating disks, while the broad H I absorption lines (e.g., fast H I outflows) are only found in high-power radio AGNs or mergers. For the low-power radio AGNs, the number of observed sources with $\log(P_{1.4\text{ GHz}}/\text{W Hz}^{-1}) < 23$ is smaller than that of brighter sources with $\log(P_{1.4\text{ GHz}}/\text{W Hz}^{-1}) > 25$ by a factor of ~ 4 (Maccagni et al. 2017; Murthy et al. 2021). It is unclear whether these previous results reveal the nature of H I absorption in low-power sources or have a bias due to the flux-limited sample. Furthermore, larger samples and more observations of low-power radio sources are needed to help understand what drives the observational differences of the H I absorption properties between low-power and high-power sources. In particular, comparisons among sources of all radio powers can provide critical information to study the interplay between the radio activity of AGN and the surrounding ISM. Thus, a systematic search of H I absorption lines in faint AGNs will help understand the possible variations of detection rate, gas properties, and kinematics along radio powers. In addition, further study with the faint AGN sample will help explore the connection between the radio power of the AGN and H I outflows/fueling. On the other hand, detailed observations with high spatial resolution can provide information on the origins and impacts of H I absorbing gas in low-power AGNs, which may help in investigating various underlying physical processes of the H I absorptions and AGN activity between low-power and high-power sources.

Constructed as the most sensitive single-dish radio telescope, the Five-hundred-meter Aperture Spherical radio Telescope (FAST; Nan 2006; Nan et al. 2011; Jiang et al. 2020) has made significant progress in probing the faintest H I gas in our Milky Way (Hong et al. 2022) and the nearby universe (Zhu et al. 2021; Xu et al. 2022). FAST has also successfully carried out a blind search and targeted observations of H I 21 cm absorption lines (Zhang et al. 2021; Hu et al. 2023; Jing et al. 2023). Recently, Yu et al. (2022) discovered a new H I absorber in an interacting galaxy pair observed by FAST. The newly detected H I absorption line has a very faint radio continuum as background (Yu et al. 2022), which shows the ability of FAST to search the H I absorption toward the faint sources. Hence, we are carrying out a systematic survey of H I absorption lines in low-power radio AGNs. In this paper, we present our results from pilot observations of the survey.

This paper is organized as follows. In Section 2, we introduce the selection of the low-power radio AGN sample, observations with FAST, and data reduction. The main results are presented in Section 3, which includes the detection rate of the H I absorption lines and properties of individual detections. In Section 4, we further discuss the results of this

study. Finally, we summarize the main results in Section 5. Throughout this paper, we adopt $H_0 = 70 \text{ km s}^{-1} \text{ Mpc}^{-1}$, $\Omega_M = 0.3$, and $\Omega_\Lambda = 0.7$.

2. Observations and Data Reduction

The three H I absorbers were newly discovered through our pilot FAST PI program (PT2021_0067 PI: Q. Yu). To investigate the H I absorption properties of low-power radio AGNs, we selected the targets by cross-matching the NRAO Very Large Array (VLA) Sky Survey (NVSS) catalog (Condon et al. 1998) and the Sloan Digital Sky Survey Data Release 16 (SDSS DR16) catalog of galaxies (Ahumada et al. 2020). We selected all sources that have radio flux of $10 \text{ mJy} < S_{1.4\text{ GHz}} < 30 \text{ mJy}$ to expand the sample of radio AGNs presented in Maccagni et al. (2017). We restricted the redshift of sources to $z < 0.1$ to avoid strong radio frequency interference (RFI). We crossmatched the selected sources with the second data release of HI-MaNGA (Stark et al. 2021) and Arecibo Legacy Fast Arecibo L-Band Feed Array Survey (ALFALFA) catalogs (Haynes et al. 2018) to exclude the sources that already have H I 21 cm emission line detections at $S/N > 5$. With the above constraints, we have compiled a sample of 159 low-power radio AGNs. In our pilot observations, 29 sources in the radio power range of $\log(P_{1.4\text{ GHz}}/\text{W Hz}^{-1}) = 21.8 - 23.7$ were observed in 2021 August to 2022 May with the FAST 19-beam receiver using the ON-OFF mode. The OFF-target position was set to $11'5$ to avoid contamination of radio continuum sources. With a beam size of $\sim 2'9$, the 19-beam receiver was configured with the wide-band spectrometer (Spec(W)) to cover a band of 1.05–1.45 GHz with a spectral resolution of $\sim 1.6 \text{ km s}^{-1}$. The integration time varies in the range of 3–21 minutes for each source based on the flux of the radio continuum at 1.4 GHz (Condon et al. 1998). Our observations are designed to reach a depth comparable to those in previous surveys (Geréb et al. 2015; Maccagni et al. 2017), which are sensitive enough to detect absorption lines with a peak optical depth of $\tau_{\text{peak}} \sim 0.08$.

Data were reduced with `astropy` (Astropy Collaboration et al. 2013) and `scipy` (Virtanen et al. 2020). We first calibrated the spectrum with the injected noise signal to derive the antenna temperature (Jiang et al. 2020). After checking the consistency of polarization XX and YY for each spectrum, we combined the two polarizations. Then the band-pass subtraction was applied with calibrated ON-target and OFF-target spectra. The temperature of each spectrum was converted to flux density based on the gain factor of different beams on the receiver (see Table 5 of Jiang et al. 2020). We subtracted the baseline of the spectrum by fitting a sinusoidal plus a polynomial function. RFI was flagged manually during the subtraction process, and we excluded the RFI-contaminated data in later works of spectral line fitting

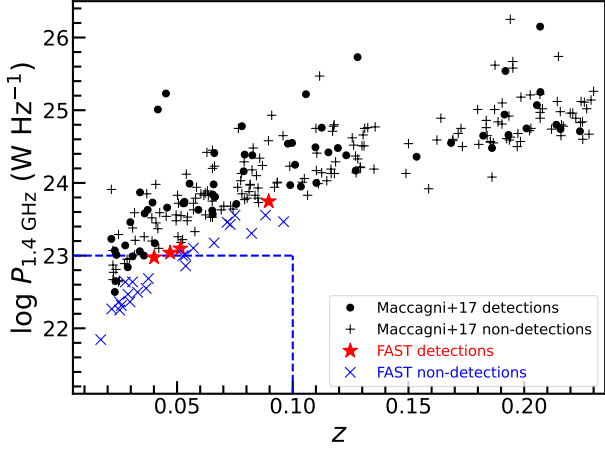


Figure 1. Comparison of the radio power and redshift between our observed sources and that of Maccagni et al. (2017).

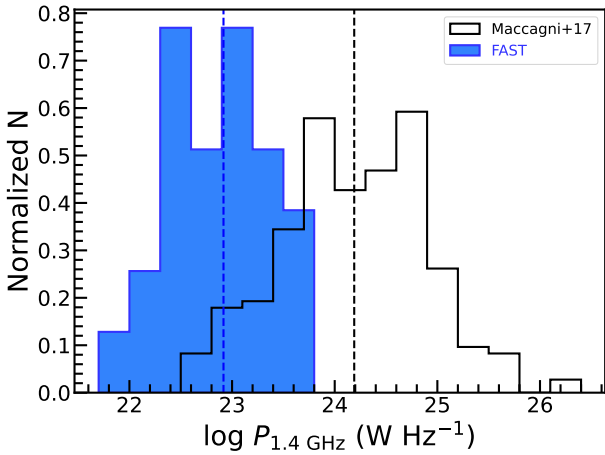


Figure 2. Distributions of the radio power of our sample and that of Maccagni et al. (2017).

and measurement. The velocity of the final spectrum was Doppler corrected and converted to the barycentric frame. After data reduction, our observations achieved a median rms noise of ~ 0.63 mJy measured at the velocity resolution of ~ 1.6 km s $^{-1}$. For the detections, we have rebinned the spectrum to improve the S/N, and the final rms noise is ~ 0.31 – 0.40 mJy at the velocity resolution of ~ 10 – 20 km s $^{-1}$ (Table 1). For the non-detections, the median rms noise is 0.19 mJy at the velocity resolution of ~ 16 km s $^{-1}$. Although the longest integration time of individual sources is less than a half hour, the average noise level of our observations is lower than previous surveys (e.g., Geréb et al. 2015; Maccagni et al. 2017) by a factor of 4 at similar spectral resolutions.

In the following analysis, we also include an HI absorber in an interacting galaxy pair J1558+2759 previously discovered by FAST (Yu et al. 2022) to investigate the gas prop-

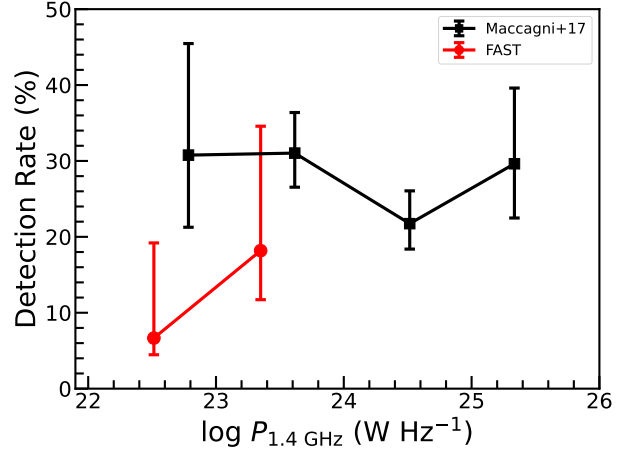


Figure 3. Comparison of the detection rate between our sample and that of Maccagni et al. (2017). The detection rates of each sample are divided into 4 bins based on the radio power. The 4 bins are (1) $\log(P_{1.4 \text{ GHz}}/\text{W Hz}^{-1}) < 23$; (2) $23 \leq \log(P_{1.4 \text{ GHz}}/\text{W Hz}^{-1}) < 24$; (3) $24 \leq \log(P_{1.4 \text{ GHz}}/\text{W Hz}^{-1}) < 25$; (4) $\log(P_{1.4 \text{ GHz}}/\text{W Hz}^{-1}) \geq 25$.

erties and origins in Section 4. This HI absorption line has a low-power radio AGN as a background continuum source similar to these three absorbers. Therefore, we discuss the HI gas properties using the new FAST observations and previous data in Yu et al. (2022). However, considering the different observing setups between the new and previous observations, we only include the 29 sources in the pilot observations to discuss the detection rate of HI absorption lines (Section 3).

In Figure 1, we plot the distributions of our observed sources and sources detected by Maccagni et al. (2017) in the radio power-redshift space for comparison. Compared to sources in Maccagni et al. (2017), the radio power of our sample is systematically lower than that of AGNs at similar redshifts, and the detected HI absorbers in our sample are among the weakest of detections at given redshifts. The blue dashed lines marked the region of $\log(P_{1.4 \text{ GHz}}/\text{W Hz}^{-1}) < 23$ and $z < 0.1$, which has been less explored in previous surveys. In the radio power range of $\log(P_{1.4 \text{ GHz}}/\text{W Hz}^{-1}) < 23$, our observations have increased the number of observed sources by a factor of 2. As shown in Figure 2, we present the histograms of the radio power range for our sample and that of Maccagni et al. (2017). The radio power of our sample distributes in the range of $\log(P_{1.4 \text{ GHz}}/\text{W Hz}^{-1}) = 21.8$ – 23.7 , and the median value of our sample ($\log(P_{1.4 \text{ GHz}}/\text{W Hz}^{-1}) = 22.9$) is lower than that of Maccagni et al. (2017) ($\log(P_{1.4 \text{ GHz}}/\text{W Hz}^{-1}) = 24.2$). Briefly, through observations of our sample, we aim to explore the HI absorption line in the faint radio AGN population, which has been less investigated in previous observations. Compared with previous observations (Geréb et al. 2015; Maccagni et al. 2017), our FAST observations on aver-

age have explored lower radio powers by ~ 0.4 dex at given redshifts (Figure 1).

3. Results

The pilot observations presented in this work yield the detection of new H I absorption lines in three galaxies with $S/N > 4.5$. The detection of new H I absorbers suggests our observations can reach the sensitivity limit of absorption lines with the peak optical depth of $\tau_{peak} \sim 0.04$. Excluding three sources severely contaminated by the RFI, our pilot observations detected H I absorption lines in three out of 26 sources, suggesting a detection rate of H I absorption lines in low-power radio AGNs that is $\sim 11.5^{+9.2}_{-3.7}\%$ in the radio power range of $\log(P_{1.4\text{ GHz}}/\text{W Hz}^{-1}) = 21.8 - 23.7$. The detection rate is relatively lower than that of previous surveys (Geréb et al. 2015; Maccagni et al. 2017), but the difference is not significant ($< 2\sigma$).

To investigate possible variations of the detection rate with the radio power, we plot the detection rate of our sample and that of Maccagni et al. (2017) along the radio power in Figure 3. The sources of each sample were divided into 4 bins based on radio powers, and the detection rate was calculated for each radio power bin. Since the sizes of subsamples in each bin are different and some are relatively small, we estimate the 1σ error bars based on the binomial statistics of Cameron (2011). The results of Maccagni et al. (2017) suggest the detection rate is similar along the entire range of radio powers in their survey. In contrast, our sample shows a lower detection rate in the radio power range of $\log(P_{1.4\text{ GHz}}/\text{W Hz}^{-1}) < 23$. As shown in Figure 3, the detection rate of sources with $\log(P_{1.4\text{ GHz}}/\text{W Hz}^{-1}) < 23$ from Maccagni et al. (2017) is higher than the detection rate of our sources ($\sim 6.7^{+12.5}_{-2.2}\%$) by a factor of ~ 4.6 . Although the difference between these two subsamples is not significant ($< 3\sigma$) considering the error bars, it is worth further investigating with larger samples to confirm whether the low-power radio AGNs with $\log(P_{1.4\text{ GHz}}/\text{W Hz}^{-1}) < 23$ have a lower detection rate of H I absorption. In the radio power range of $23 \leq \log(P_{1.4\text{ GHz}}/\text{W Hz}^{-1}) < 24$, the detection rate of our sample is consistent with that of Maccagni et al. (2017) within the error bars. Our results indicate that the low-power sources with $\log(P_{1.4\text{ GHz}}/\text{W Hz}^{-1}) < 23$ may have a lower detection rate of H I absorption, and the detection rate increases and remains similar as the radio power elevating.

As shown in Figure 4, two H I absorbers present multi-peak profiles, and each peak is identified with an $S/N > 3$. Therefore, we have performed a multicomponent Gaussian fit to measure the properties of each absorption line. In the multicomponent Gaussian models, we decided the number of components by requiring the reduced χ^2 to be closest to unity. We have checked the Akaike information criterion (AIC) between a single Gaussian fit and a multi-Gaussian fit,

and the AIC suggests the multi-Gaussian model can better fit the data. The χ^2 , degree of freedom (d.o.f.), and AIC of both single-component and multicomponent Gaussian fits are listed in Table 2. The results of multicomponent Gaussian fit revealed the asymmetric shape of the line profiles, indicating the absorbing gas may have multiple velocity components. However, these components still need to be confirmed with higher spectral resolution and S/N . We summarize the measured parameters and the results of multicomponent Gaussian fit in Table 1 and Table 3, respectively. The line width W_{20} is measured at 20% of peak flux density for each Gaussian fit profile, and the line centroids of each absorption system are measured at the center point of W_{20} . The column density is calculated with the following equation:

$$N_{\text{HI}} = 1.823 \times 10^{18} T_s \int \tau(v) dv \text{ cm}^{-2}, \quad (1)$$

where T_s represents the spin temperature in Kelvin, and v is the Doppler-corrected velocity in kilometer per second. The optical depth $\tau(v)$ is derived by:

$$\tau(v) = -\ln \left(1 + \frac{S_{\text{HI}}}{c_f S_{1.4\text{ GHz}}} \right), \quad (2)$$

where S_{HI} is the line flux of the H I absorption, $S_{1.4\text{ GHz}}$ is the continuum flux at 1.4 GHz, and c_f is the covering factor of the gas. In this work, we assume the spin temperature $T_s = 100$ K and the covering factor $c_f = 1$ for each source, which has been commonly adopted in previous studies (e.g., Geréb et al. 2015; Maccagni et al. 2017; Chowdhury et al. 2020).

3.1. J1332+2634

The source J1332+2634 is an isolated galaxy with a spectroscopic redshift of $z = 0.04701 \pm 0.00002$ (Ahumada et al. 2020). The host galaxy is a star-forming galaxy with a low stellar mass of $\log(M_*/M_\odot) = 9.7$ and star formation rate (SFR) of $3.1 M_\odot \text{ yr}^{-1}$ (Salim et al. 2016). J1332+2634 is classified as a Seyfert 2 AGN (Toba et al. 2014) and has a flux of 21.1 mJy at 1.4 GHz (Condon et al. 1998). The corresponding radio power at 1.4 GHz is $\log(P_{1.4\text{ GHz}}/\text{W Hz}^{-1}) = 23.04$.

The H I absorption line profile of J1332+2634 is shown in Figure 4, with the velocity Doppler corrected based on the optical redshift of the host galaxy. The detected H I absorption line presents a multi-peak profile, implying unsettled kinematics of the absorbing gas. Fitted with a multicomponent Gaussian function, the line profile is decomposed into three velocity components centered at -72.0 km s^{-1} , -20.5 km s^{-1} , and 10.0 km s^{-1} , respectively. Despite the shallower blueshifted wing component, the velocity of the

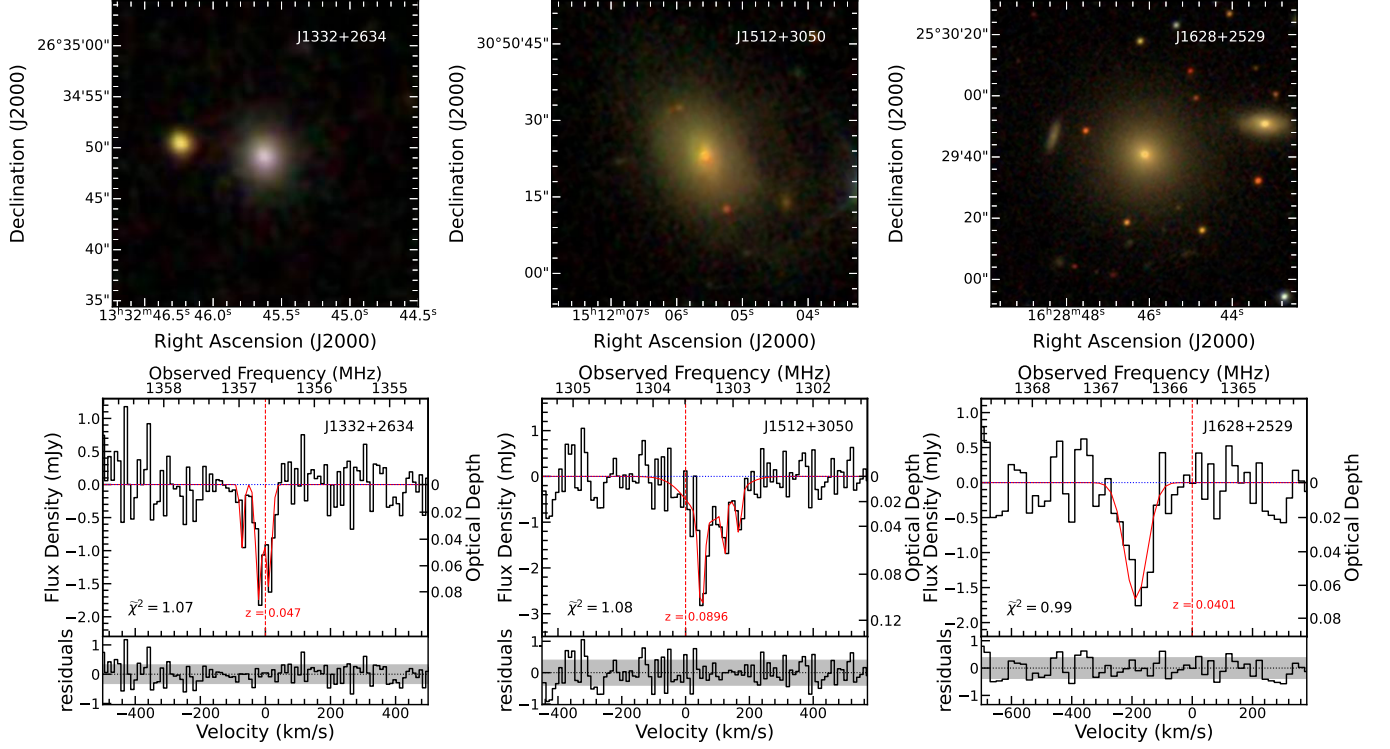


Figure 4. The upper panels show SDSS composite images of each source. The FAST beam size ($\sim 2''.9$) is much larger than the size of these optical images. The lower panels show the corresponding H I spectra of J1332+2634, J1512+3050, and J1628+2529. The velocity resolution of J1332+2634 and J1512+3050 is $\sim 10 \text{ km s}^{-1}$, while the spectrum of J1628+2529 is rebinned to $\sim 20 \text{ km s}^{-1}$. The red lines in each panel show the profiles of Gaussian fits. On the bottom of each panel, the residuals of the fit are plotted with the 1σ noise values presented with shaded regions.

absorption system is in good agreement with the optical redshift of the host galaxy, suggesting the dominant components are likely tracing the circumnuclear rotating disk (Gallimore et al. 1999). The blueshifted wing centered at -72.0 km s^{-1} has a narrow profile with an FWHM of 13.5 km s^{-1} . Adopting a 21.1 mJy continuum flux density at 1.4 GHz (Condon et al. 1998), we calculate the peak optical depth $\tau_{\text{peak}} = 0.091 \pm 0.017$ and the integrated optical depth $\tau_{\text{int}} = 4.91 \pm 0.67 \text{ km s}^{-1}$. Based on Equation (1), the column density of this absorption system is $\sim 8.95 \times 10^{20} \text{ cm}^{-2}$.

3.2. J1512+3050

The source J1512+3050 is an isolated galaxy with the spectroscopic redshift of $z = 0.08963 \pm 0.00002$ (Ahumada et al. 2020). The host galaxy is an elliptical galaxy with a high stellar mass of $\log(M_*/M_\odot) = 11.7$ (Salim et al. 2016). Classified as a LINER-type AGN (Toba et al. 2014), J1512+3050 has a 1.4 GHz continuum flux of 27.8 mJy (Condon et al. 1998), corresponding to a radio power at 1.4 GHz of $\log(P_{1.4 \text{ GHz}}/\text{W Hz}^{-1}) = 23.74$.

As shown in Figure 4, the H I absorption line profile of J1512+3050 is Doppler corrected based on the optical redshift of the host galaxy. The multiple-peak profile of the H I absorption line suggests the H I gas is kinematically unset-

tled. A multicomponent Gaussian fit yields the peak optical depth $\tau_{\text{peak}} = 0.107 \pm 0.019$ and the integrated optical depth $\tau_{\text{int}} = 8.81 \pm 0.81 \text{ km s}^{-1}$. The column density N_{HI} of this absorption system based on Equation (1) is $\sim 1.61 \times 10^{21} \text{ cm}^{-2}$. The line profile is decomposed into one broad component centered at 74.9 km s^{-1} , and three narrow Gaussian components centered at 49.7 km s^{-1} , 120.2 km s^{-1} , and 167.5 km s^{-1} , respectively. The fitting parameters of each Gaussian component are listed in Table 3. The redshifted wings may suggest the H I gas is clumpy and falling toward the AGN.

3.3. J1628+2529

The source J1628+2529 is a member galaxy in a galaxy group with a spectroscopic redshift of $z = 0.04010 \pm 0.00001$ (Ahumada et al. 2020). The host galaxy is an elliptical galaxy with a high stellar mass of $\log(M_*/M_\odot) = 11.1$ (Salim et al. 2016). Classified as a LINER-type AGN (Jeong et al. 2013), J1628+2529 has a 1.4 GHz continuum flux of 25.2 mJy (Condon et al. 1998), corresponding to a radio power at 1.4 GHz of $\log(P_{1.4 \text{ GHz}}/\text{W Hz}^{-1}) = 22.98$.

As shown in Figure 4, the H I absorption line profile of J1628+2529 is Doppler corrected and rebinned to a velocity resolution of 20 km s^{-1} , and the zero-point is corrected

Table 1. Absorption line properties

Source name	R.A.	Decl.	t_{ON}	z	$S_{1.4\text{ GHz}}$	$\log(P_{1.4\text{ GHz}})$	rms	Δv	W_{20}	v_{centroid}	τ_{peak}	τ_{int}	N_{HI}
	deg.	deg.	(min)		(mJy)	(W Hz ⁻¹)	(mJy)	(km s ⁻¹)	(km s ⁻¹)	(km s ⁻¹)		(km s ⁻¹)	(10 ²⁰ cm ⁻²)
(1)	(2)	(3)	(4)	(5)	(6)	(7)	(8)	(9)	(10)	(11)	(12)	(13)	(14)
J1332+2634	203.19009	26.58038	5	0.04701	21.1	23.04	0.31	10	106.9	-26.8	0.091 ± 0.017	4.91 ± 0.67	8.95 ± 1.22
J1512+3050	228.02324	30.83984	6.5	0.08963	27.8	23.74	0.40	10	172.7	93.0	0.107 ± 0.019	8.81 ± 0.81	16.06 ± 1.48
J1558+2759 ^a	239.75275	27.98537	13	0.05140	20.0	23.10	0.44	1.6	72.3	125.3	0.490 ± 0.050	14.50 ± 0.32	47.30 ± 1.01
J1628+2529	247.19221	25.49472	3.3	0.04010	25.2	22.98	0.38	20	131.6	-195.9	0.072 ± 0.017	6.46 ± 0.97	11.78 ± 1.77

Notes. The columns are (1) the source name of the AGN; (2) R.A. in degrees; (3) Decl. in degrees; (4) integration time; (5) redshift from SDSS spectroscopy (Abolfathi et al. 2018); (6) radio continuum flux at 1.4 GHz from NVSS (Condon et al. 1998); (7) radio power at 1.4 GHz; (8) 1σ noise measured at re-binned velocity resolution; (9) re-binned velocity resolution; (10) line width measured at 20% of the peak flux; (11) line centroid of the absorption; (12) peak optical depth; (13) integrated optical depth; (14) estimated HI column density assuming $T_s = 100$ K, $c_f = 1$.

^a The detailed data and measurements of this source are adopted from Yu et al. (2022).

Table 2. Comparison of single and multiple Gaussian fits for the multi-peak HI absorbers

Source name	χ^2_{single}	d.o.f. _{single}	AIC _{single}	χ^2_{multi}	d.o.f. _{multi}	AIC _{multi}
(1)	(2)	(3)	(4)	(5)	(6)	(7)
J1332+2634	270.3	237	34.5	247.0	231	24.9
J1512+3050	136.0	100	34.6	98.7	91	19.6

Notes. The columns are (1) the source name of the AGN; (2) χ^2 of the single-component Gaussian fit; (3) the degree of freedom (d.o.f.) of the single-component Gaussian fit; (4) Akaike information criterion (AIC) of the single-component Gaussian fit; (5) χ^2 of the multi-component Gaussian fit; (6) d.o.f. of the multi-component Gaussian fit; (7) AIC of the multi-component Gaussian fit.

to the optical redshift of the host galaxy. Since this HI absorption line shows a single-peak profile, we apply a single-component Gaussian fit to measure the peak optical depth $\tau_{\text{peak}} = 0.072 \pm 0.017$ and the integrated optical depth $\tau_{\text{int}} = 6.46 \pm 0.97$ km s⁻¹. Based on Equation (1), the column density N_{HI} of this absorption system is $\sim 1.18 \times 10^{21}$ cm⁻². The line centroid is blueshifted ~ -196 km s⁻¹ with respect to the systemic velocity of the host galaxy. Although the line width of this absorber is relatively narrow with a blueshifted centroid, it is likely the associated absorption of the AGN, considering the high column density. Since the velocity of the absorption line is significantly blueshifted, the HI absorption with high column density may suggest the case of gas outflowing from the AGN.

4. Discussions

4.1. Detection Rate

Table 3. Gaussian fit parameters of the multi-peak HI absorbers

Source name	FWHM	v_{centroid}	S/N _{peak}	τ_{peak}	τ_{int}	N_{HI}
	(km s ⁻¹)	(km s ⁻¹)			(km s ⁻¹)	(10 ²⁰ cm ⁻²)
(1)	(2)	(3)	(4)	(5)	(6)	(7)
J1332+2634	22.5	10.0	5.9	0.075	1.79 ± 0.47	3.26 ± 0.85
	21.0	-20.5	5.9	0.085	1.89 ± 0.47	3.44 ± 0.85
	13.5	-72.0	3.0	0.046	0.67 ± 0.35	1.22 ± 0.63
J1512+3050	21.1	49.7	7.1	0.091	2.32 ± 0.58	4.23 ± 1.06
	153.6	74.9	-	0.047	7.68 ± 1.36	14.00 ± 2.48
	6.9	120.2	4.2	0.046	0.72 ± 0.41	1.31 ± 0.74
	17.7	167.5	3.0	0.041	0.81 ± 0.57	1.48 ± 1.04

Notes. The columns are (1) the source name of the AGN; (2) full width at half maximum; (3) line centroid of the absorption component; (4) the S/N of identified peak in the spectrum; (5) peak optical depth; (6) integrated optical depth; (7) estimated HI column density assuming $T_s = 100$ K, $c_f = 1$.

The pilot observations of HI absorption lines suggest a detection rate of $\sim 11.5^{+9.2}_{-3.7}\%$ in the sample of 26 low-power radio sources, and sources with $\log(P_{1.4\text{ GHz}}/\text{W Hz}^{-1}) < 23$ present a lower detection rate of $\sim 6.7^{+12.5}_{-2.2}\%$. Considering the uncertainties, the detection rate of HI absorption in lower-power sources is relatively lower than that of previous targeted surveys through direct comparisons (van Gorkom et al. 1989; Emonts et al. 2010; Chandola et al. 2011; Geréb et al. 2015; Maccagni et al. 2017). However, a fair comparison of detection rates between surveys requires comparable detection limits and considerations of selection bias.

Since the representative sample observed by WSRT (Geréb et al. 2014, 2015; Maccagni et al. 2017) has overlapped regions with our sample in the radio power-redshift space (see Figure 1), the comparison between our sample and the WSRT

sample under similar detection limits is reasonable and helpful to investigate the detection rate of low-power sources. In Figure 5(C), we presented the upper limits of peak optical depth (τ_{peak}) for non-detections in both our sample and the WSRT sample (Maccagni et al. 2017). The upper limits of τ_{peak} were estimated with 3σ rms noise (Table A1) at the velocity resolution of $\sim 16 \text{ km s}^{-1}$ based on Equation (2). Our observations achieved a median τ_{peak} upper limit of ~ 0.04 , which is similar to that of the WSRT observations (~ 0.04 , Maccagni et al. 2017). Thus, the detection limit of FAST observations is similar to that of Maccagni et al. (2017).

Apart from the detection limit, selection effects can also significantly impact the detection rate of H I absorption lines. Previous studies have revealed that a large fraction of early-type galaxies harbors amounts of detectable H I gas (Oosterloo et al. 2010; Serra et al. 2012). Therefore, the elimination of gas-rich sources in the AGN sample will decrease the detection probability of H I absorption and reduce a large fraction of the parent population. In the selection of our parent sample, we excluded sources that already have H I emission detections ($S/N > 5$) to reduce redundant observations, because FAST observations focus on searching H I absorption lines to build up an H I absorption sample of faint radio AGNs. After crossmatching with HI-MaNGA DR2 and ALFALFA catalogs, we excluded 19 out of 180 sources in the parent sample, corresponding to approximately two to three potentially excluded sources in the pilot observations. The rest sources of the parent sample were not observed by either HI-MaNGA or ALFALFA, and the sample still contains a certain amount of gas-rich ($\sim 35\%$) galaxies based on SDSS spectra. The potential exclusion of two to three H I-rich sources could reduce the chance of detecting new H I absorption lines in the sample, which may underestimate the detection rate. Therefore, the H I absorption detection rate of $11.5_{-3.7}^{+9.2}\%$ can be considered as the lower limit for our sample. For sources with $\log(P_{1.4 \text{ GHz}}/\text{W Hz}^{-1}) < 23$, the H I absorption detection rate of $6.7_{-2.2}^{+12.5}\%$ could also represent the lower limit.

For our sample observed by FAST, the H I emission and the radio morphology of sources may reduce the likelihood of detecting H I absorption. Since the H I emission becomes more detectable at a lower redshift, the lower detection rate of H I absorption may be partly due to the dilution by H I emission (Allison et al. 2014; Curran & Duchesne 2018). In the selection of the parent sample, most of the excluded gas-rich sources distribute at lower redshifts ($z < 0.03$), and their potential H I absorptions could be diluted by H I emission. In addition, previous studies have found the detection rate of H I absorption in compact sources is higher than that in extended sources (e.g., Maccagni et al. 2017). We followed Geréb et al. (2015) and Maccagni et al. (2017) to inspect our sources, and the classification results suggest our sam-

ple has a large fraction of extended radio sources ($\sim 65\%$, Table A1), which may also lead to the observed lower detection rate. Our sample has nine compact sources ($\sim 35\%$) with two detected absorptions, and one detection out of 17 extended sources ($\sim 65\%$). The detection rate of the compact sources in our sample ($22.2_{-8.1}^{+18.3}\%$) is consistent with that of Maccagni et al. (2017) within error bars. Considering the uncertainties, the detection rate of the extended sources in our sample ($5.9_{-1.9}^{+11.3}\%$) is consistent with that of Maccagni et al. (2017). Therefore, the lower detection rate of H I absorption in FAST observations may be due to the dilution by H I emission at lower redshift and the selection of more extended sources.

Thus, as a reasonable comparison of detection rates between our sample and the WSRT sample, our observations suggest a lower detection rate of H I absorption lines in the low-power radio sources. Due to the incompleteness of the sample, these detection rates may represent the lower limits. The selection of more extended sources and dilution by H I emission at lower redshift may contribute to the lower detection rate of H I absorption lines. One caveat of this result is the fact that the detection rate could be affected by low number statistics, which will be further investigated with the complete survey of the parent sample.

4.2. Kinematics and the Origin of the Absorbing Gas

To investigate the origin of H I 21 cm absorption, many studies have used high spatial resolution interferometry observations to explore the detailed kinematics and structures of the absorption. These observations have found evidence of various probabilities that can form H I absorption in radio AGNs: rotating gas disks (Gallimore et al. 1999; Morganti et al. 2008; Struve & Conway 2010), high-velocity clouds (HVCs; Conway 1999; Struve & Conway 2012), gas outflows (Morganti et al. 2013; Schulz et al. 2021), and gas falling toward the supermassive black hole (Morganti et al. 2009; Maccagni et al. 2014; Tremblay et al. 2016). Based on these observations, the origin and related mechanisms of the H I absorption can be discussed by analyzing the line profiles and kinematics of the absorbing gas. Alternatively, since the absorption line traces the foreground gas along the line of sight of the continuum source, the morphology and structure of the radio continuum can also contribute to the observed absorption profiles (Murthy et al. 2021).

Figure 5(A) shows the W_{20} of the H I absorption lines versus the radio power of the sources. Maccagni et al. (2017) has found that broad lines ($W_{20} > 400 \text{ km s}^{-1}$) were only detected in the interacting galaxies at low radio power ($\log(P_{1.4 \text{ GHz}}/\text{W Hz}^{-1}) < 24$). The line widths of the new H I absorbers detected by FAST are relatively narrow and consistent with the results of Maccagni et al. (2017). One of our sources is discovered in a merging galaxy pair (Yu et al.

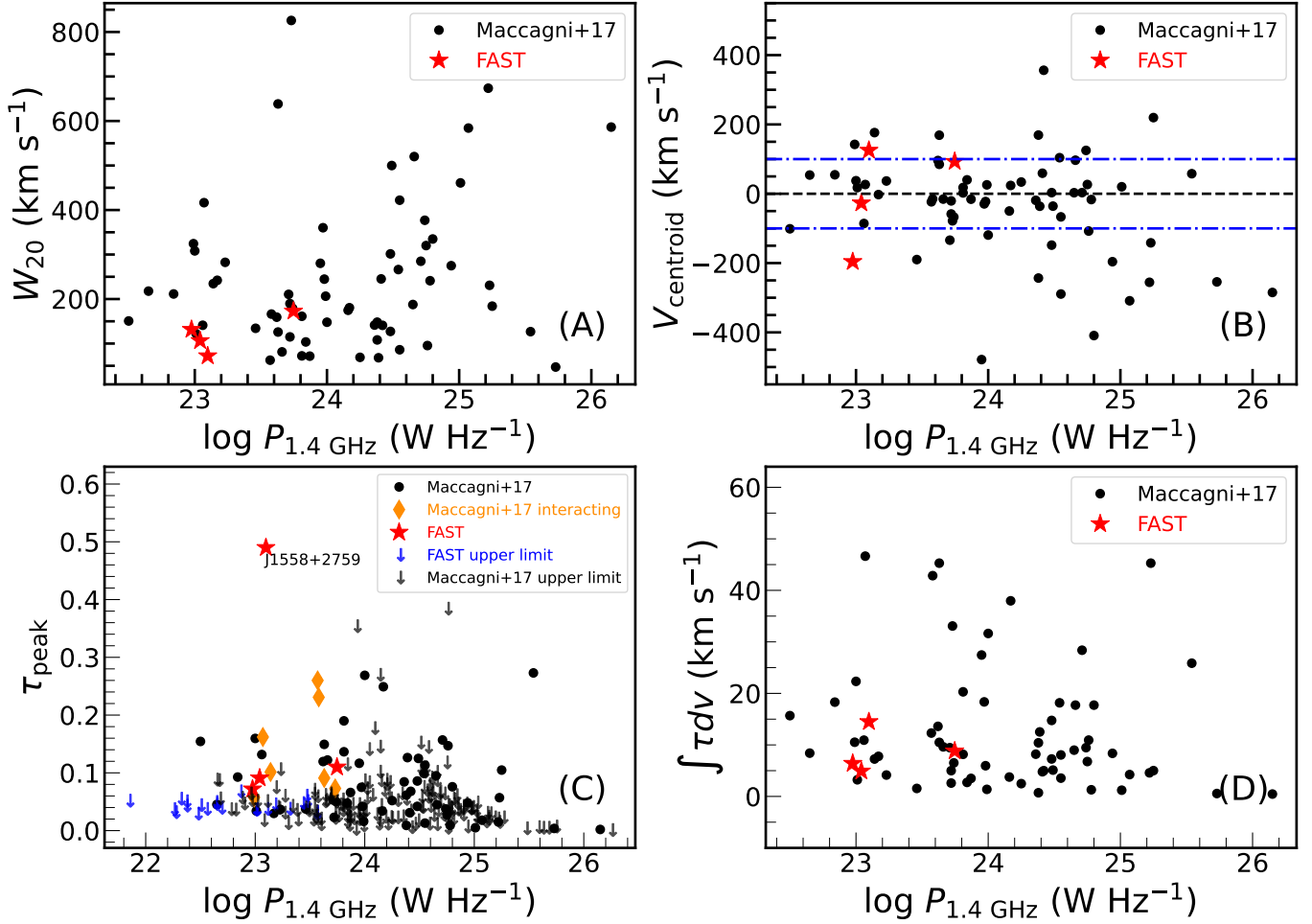


Figure 5. (A) Line width measured at 20% of the intensity (W_{20}) of the HI profiles vs. the radio power of the sources. (B) Line centroid offset with respect to the systemic velocity vs. the radio power of the sources. The fine dashed lines in blue show the interval of $\pm 100 \text{ km s}^{-1}$. (C) Peak optical depth vs. the radio power of the sources. The interacting sources of Maccagni et al. (2017) are marked with orange diamonds. (D) Integrated optical depth vs. the radio power of the sources.

2022), and comparable narrow lines also have been detected in the interacting sources (Maccagni et al. 2017; Dutta et al. 2019). In Figure 5(B), we plot the centroid shift of the line with respect to the galaxy’s systemic velocity versus the radio power of the sources. The fine dashed lines in blue show the interval of $\pm 100 \text{ km s}^{-1}$. Maccagni et al. (2017) suggests the majority of the lines detected in low-power sources are centered at the systemic velocity ($|\Delta v| < 100 \text{ km s}^{-1}$), while two of four in our FAST detected sources are offset relative to the systemic velocity. For the source J1512+3050, although the systemic centroid of the absorbing gas is $\sim 93 \text{ km s}^{-1}$, it still has two narrow components redshifted more than 100 km s^{-1} . Our detections have a high fraction of sources with large velocity offset ($|\Delta v| > 100 \text{ km s}^{-1}$), which may suggest various kinematics and possible connections to the inflows and outflows of the gas.

Previous observations suggest the HI 21cm absorption originated from rotating disks generally have symmetric pro-

files and line widths of a few hundred km s^{-1} , centered at or close to the systemic velocity (Gallimore et al. 1999; Murthy et al. 2021). The absorption lines associated with gas outflows usually show broad and asymmetric profiles, and the line centroid is blueshifted from the systemic velocity (Morganti et al. 2013; Schulz et al. 2021). Relatively narrow redshifted profiles may originate from gas clouds falling into the SMBH (Morganti et al. 2009; Maccagni et al. 2014). Alternatively, HVCs along the line of sight can also be observed as narrow HI absorption lines (Conway 1999; Araya et al. 2010). Besides, the structures (e.g., core, jets, or lobes) of the background continuum source may partially align with the HI gas, which can result in the multiple velocity components and asymmetries observed in the absorption profiles (Peck & Taylor 2001; Struve et al. 2010; Murthy et al. 2021). In particular, for the radio AGN with the typical two-jetted structure, since one jet is often behind the HI gas, the jet-cloud alignment can produce asymmetric or velocity-shifted

absorption profiles even if the H I disk and radio continuum both have symmetric morphologies.

The H I absorption profile of J1332+2634 shows a symmetric shape of the main component centered at the systemic velocity of the host galaxy, which indicates that a rotating disk very likely contributes the majority of absorption. However, J1332+2634 presents a shallower narrow wing centered at -72.0 km s^{-1} , with a column density of $\sim 1.22 \times 10^{20} \text{ cm}^{-2}$. Since confirmed H I outflows generally present broad profiles with large blueshifted velocity, the narrow wing of absorption in J1332+2634 likely traces an intermediate velocity cloud (IVC). Additionally, with spatially unresolved observations, we cannot rule out the scenario that the observed wing component or asymmetric absorption profile may be due to structures of the radio continuum, so the foreground H I gas could distribute in a regular rotating disk.

The absorption profile of J1512+3050 presents an asymmetric multi-peak shape, redshifted with respect to the systemic velocity of the host galaxy. These two shallower redshifted components show narrow profiles with column densities of $\sim 1.31 \times 10^{20} \text{ cm}^{-2}$ and $\sim 1.48 \times 10^{20} \text{ cm}^{-2}$, respectively. The redshifted wings may suggest gas clouds falling onto the SMBH, which is correlated to the feeding and triggering of AGN. Alternatively, clumpy HVCs along the line of sight may also produce the presented absorption profile. Considering the possible partial alignment between the continuum structures (e.g., lobes) and the H I cloud, the warped H I could also present such features (Murthy et al. 2021).

The absorption profile of J1628+2529 shows a narrow blueshifted shape, and the offset relative to systemic velocity is -195.9 km s^{-1} . Although the line width of the absorption is relatively narrow compared to the broad lines revealed by previous observations (e.g., Morganti et al. 2013; Schulz et al. 2021), gas outflows from the AGN could be the possible origin. In particular, observations at higher redshift have discovered a narrow ($\sim 40 \text{ km s}^{-1}$) blueshifted H I line that traced the outflows driven by the radio jet (Aditya et al. 2017). As shown in Figure 5(B), low-power radio sources ($\log(P_{1.4 \text{ GHz}}/W \text{ Hz}^{-1}) < 24$) with large blueshifted velocity offsets are relatively rare compared to high-power radio sources ($\log(P_{1.4 \text{ GHz}}/W \text{ Hz}^{-1}) > 24$). Especially, for sources with $\log(P_{1.4 \text{ GHz}}/W \text{ Hz}^{-1}) < 23$, J1628+2529 is the only detection of sources with large blueshifted velocity offsets ($\Delta v < -100 \text{ km s}^{-1}$). If the H I absorption line of J1628+2529 is confirmed to be outflows, it could be the lowest radio power source with outflows. Assuming the absorbing gas to be outflows, we can estimate the mass outflow rate following Heckman (2002):

$$\dot{M}_{\text{HI}} \sim 30 \frac{r_*}{\text{kpc}} \frac{N_{\text{HI}}}{10^{21} \text{ cm}^{-2}} \frac{v}{300 \text{ km s}^{-1}} \frac{\Omega}{4\pi} M_{\odot} \text{ yr}^{-1}, \quad (3)$$

where the r_* is the radius of the outflow gas, N_{HI} is the estimated column density assuming $T_s = 100 \text{ K}$, $c_f = 1$, v is

the velocity of the outflow gas, and Ω is the solid angle of the gas assumed to be π . Since neither FAST nor VLA resolves the compact continuum source, we assume a typical upper limit radius of $r_* = 1 \text{ kpc}$ considering outflows generally appear to be limited to the central kiloparsec scale (Morganti & Oosterloo 2018). Therefore, we estimate the mass outflow rate to be $\sim 5.8 M_{\odot} \text{ yr}^{-1}$, with $N_{\text{HI}} = 1.18 \times 10^{21} \text{ cm}^{-2}$ and $r_* = 1 \text{ kpc}$. Alternatively, HVCs away from the nucleus could also result in the blueshifted absorption feature. Besides, for a typical two-jetted radio AGN, the jet-cloud alignment may give rise to the significantly blueshifted profile when one jet is behind the rotating H I disk.

Similarly, the absorption profile of J1558+2759 is narrow and redshifted, which can be contributed either by gas fueling or galactic gas clouds. Observations of H I absorptions in mergers have detected significant systemic velocity redshift, which suggests the signature of gas infall (Dutta et al. 2019). Since J1558+2759 is an interacting source, gas driven by the merging process could infall toward the AGN, which may connect with the gas fueling onto the SMBH (Srianand et al. 2015). On the other hand, HVCs or a large-scale gas disk along the line of sight can also be observed as redshifted absorption lines.

Since FAST cannot resolve these sources, spatially resolved H I observations by interferometry will help understand the kinematics and origin of the absorbing gas, as well as possible jet-ISM interactions.

4.3. Uncertainties of the Systemic Velocity

To understand the origin of the absorbing gas, the important information of gas kinematics depends on the comparison between the systemic velocity of the galaxy and the velocity of H I gas. As revealed by previous studies (e.g., Morganti et al. 2001), the uncertainties of the redshift of the galaxy could bias the derived systemic velocity and further affect our understanding of the origin of the gas.

For our detected sources, the systemic velocities are derived by optical redshift from SDSS spectroscopy. The 1σ error of the redshift is ~ 0.00002 , which corresponds to 6 km s^{-1} . Considering the spectral resolution of the profile, the line centroid of J1332+2634 is $-26.8 \pm 11.7 \text{ km s}^{-1}$, which indicates the velocity offset of H I absorption line is not significant with respect to the systemic velocity. The source J1512+3050 has a velocity offset of $93.0 \pm 11.7 \text{ km s}^{-1}$, which suggests the H I absorption line is significantly redshifted as discussed above. The line centroid of J1628+2529 is $-195.9 \pm 20.9 \text{ km s}^{-1}$, indicating the H I absorbing gas is significantly blueshifted relative to the systemic velocity. For the interacting source J1558+2759, an older study claimed a spectroscopic redshift of $z = 0.05174 \pm 0.00027$ (Kim et al. 1995), which corresponds to a larger error of 81 km s^{-1} . If the older redshift is adopted

to derive the systemic velocity, the velocity offset of the H I absorption line becomes $23.4 \pm 81.0 \text{ km s}^{-1}$. The old observations with large uncertainties could be limited by the previous instruments, while the SDSS dataset contains spatially resolved MaNGA observations, which can alleviate uncertainties from motions of emitting gas. Thus, the redshift from SDSS is likely more accurate to derive the real systemic velocity, and the source J1558+2759 is significantly redshifted with respect to the systemic velocity.

4.4. Optical Depth

In Figure 5(C) and (D), we show a comparison of the peak optical depth and the integrated optical depth of our sources with that of Maccagni et al. (2017). The peak optical depths of our sources are consistent with previous observations, except for the interacting source J1558+2759, which presents remarkably high τ_{peak} . The high τ_{peak} value of J1558+2759 is close to that of H I absorbers detected at higher redshift (Chowdhury et al. 2020). We have marked the interacting sources of Maccagni et al. (2017) with orange to check whether all the interacting sources show higher τ_{peak} values. The mean τ_{peak} value of the interacting sources (0.14 ± 0.03) is slightly higher than that of noninteracting sources (0.08 ± 0.01). In addition, a recent survey of H I absorption lines in the galaxy merger sample (Dutta et al. 2018, 2019) also reveals a few sources with higher peak optical depth ($\tau_{\text{peak}} > 0.4$). This provides a hint that galaxy interactions and mergers may have contributions to the high value of τ_{peak} . Observations and simulations suggest galaxy interactions can induce tidal torque to trigger the infall of diffuse ionized halo gas toward the central region of the galaxy, which increases the density of the ionized gas and makes the cooling more efficient (Braine & Combes 1993; Moreno et al. 2019). In this scenario, the ionized gas will turn into atomic gas, and the external pressure (e.g., shocks) induced by interactions will accelerate the transition from atomic to molecular gas (Barnes 2004; Kaneko et al. 2017), which would create a dense environment. Indeed, previous observations of H I absorption lines have detected significant high N_{HI} in mergers (Dutta et al. 2019), which may result in the high τ_{peak} of the interacting sources. For the integrated optical depth, the results of our detections are consistent with those of Maccagni et al. (2017).

5. Summary

We present pilot observations of H I absorption search toward low-power radio AGNs by FAST. With the high sensitivity of FAST, we discovered three new H I absorbers at a very weak flux level. Our pilot observations suggest the detection rate of H I absorption lines in our sample is $\sim 11.5^{+9.2}_{-3.7}\%$. Considering the uncertainties, the detection rate is slightly lower than that of brighter sources, but the

difference is not significant ($< 2\sigma$). Our results indicate that the low-power sources with $\log(P_{1.4 \text{ GHz}}/\text{W Hz}^{-1}) < 23$ may have a lower detection rate of H I absorption, and the detection rate increases and remains similar as the radio power elevating. Due to the incompleteness of the sample, these detection rates may represent the lower limits. The selection of more extended sources and dilution by H I emission at lower redshift may contribute to the lower detection rate of H I absorption lines. These detected absorbers present relatively narrow line widths and comparable column densities as revealed by previous observations of low-power radio AGNs. One absorber has a symmetric profile with a large velocity offset, while the other two absorbers show asymmetric profiles that can be decomposed into multiple components, suggesting various possibilities of gas kinematics and origins. These absorbers may have connections with rotating disks, gas outflows, galactic gas clouds, gas fueling of the AGN, and jet-ISM interactions, which needs to be confirmed or ruled out by spatially resolved observations. The upcoming systematic survey and high spatial resolution observations of the H I absorbers in low-power AGNs will shed new light on our understanding of multiple evolution processes of the faint radio AGN population.

We thank the anonymous referee for the careful reading and helpful comments that improved the paper. Q.Y. appreciates the helpful suggestions by Dr. Mouyuan Sun, and observing support from Dr. Bo Zhang. This work is supported by the National Key R&D Program of China under No. 2017YFA0402600, and the National Natural Science Foundation of China under Nos. 11890692, 12133008, 12221003. Junfeng Wang acknowledges support by the NSFC grants Nos. U1831205 and 12033004. We acknowledge the science research grants from the China Manned Space Project with Nos. CMS-CSST-2021-A04, CMS-CSST-2021-A05, CMS-CSST-2021-A06, CMS-CSST-2021-B02.

This work made use of the data from FAST (Five-hundred-meter Aperture Spherical radio Telescope). FAST is a Chinese national mega-science facility, operated by National Astronomical Observatories, Chinese Academy of Sciences.

Facilities: FAST.

Software: Astropy (Astropy Collaboration et al. 2013), Scipy (Virtanen et al. 2020), LMFIT (Newville et al. 2014).

Appendix A. Summary Table of Non-detections

We summarized the ancillary information of the H I absorption non-detections in Table A1.

References

- Abolfathi, B., Aguado, D. S., Aguilar, G., et al. 2018, *ApJS*, **235**, 42
- Aditya, J. N. H. S. 2019, *MNRAS*, **482**, 5597
- Aditya, J. N. H. S., & Kanekar, N. 2018, *MNRAS*, **473**, 59
- Aditya, J. N. H. S., Kanekar, N., Prochaska, J. X., et al. 2017, *MNRAS*, **465**, 5011
- Ahumada, R., Prieto, C. A., Almeida, A., et al. 2020, *ApJS*, **249**, 3
- Allison, J. R., Sadler, E. M., & Meekin, A. M. 2014, *MNRAS*, **440**, 696
- Araya, E. D., Rodríguez, C., Pihlström, Y., et al. 2010, *AJ*, **139**, 17
- Astropy Collaboration, Robitaille, T. P., Tollerud, E. J., et al. 2013, *A&A*, **558**, A33
- Barnes, J. E. 2004, *MNRAS*, **350**, 798
- Braine, J., & Combes, F. 1993, *A&A*, **269**, 7
- Cameron, E. 2011, *PASA*, **28**, 128
- Chandola, Y., Sirothia, S. K., & Saikia, D. J. 2011, *MNRAS*, **418**, 1787
- Chowdhury, A., Kanekar, N., & Chengalur, J. N. 2020, *ApJL*, **900**, L30
- Condon, J. J., Cotton, W. D., Greisen, E. W., et al. 1998, *AJ*, **115**, 1693
- Conway, J. E. 1999, *NewAR*, **43**, 509
- Curran, S. J., & Duchesne, S. W. 2018, *MNRAS*, **476**, 3580
- Dutta, R., & Srianand, R. 2022, *MNRAS*
- Dutta, R., Srianand, R., & Gupta, N. 2018, *MNRAS*, **480**, 947
- . 2019, *MNRAS*, **489**, 1099
- Emonts, B. H. C., Morganti, R., Struve, C., et al. 2010, *MNRAS*, **406**, 987
- Gallimore, J. F., Baum, S. A., O’Dea, C. P., et al. 1999, *ApJ*, **524**, 684
- Geréb, K., Maccagni, F. M., Morganti, R., & Oosterloo, T. A. 2015, *A&A*, **575**, A44
- Geréb, K., Morganti, R., & Oosterloo, T. A. 2014, *A&A*, **569**, A35
- Haynes, M. P., Giovanelli, R., Kent, B. R., et al. 2018, *ApJ*, **861**, 49
- Heckman, T. M. 2002, *Astronomical Society of the Pacific Conference Series*, **254**, 292
- Hong, T., Han, J., Hou, L., et al. 2022, *Science China Physics, Mechanics, and Astronomy*, **65**, 129702
- Hu, W., Wang, Y., Li, Y., et al. 2023, *A&A*, **675**, A40
- Jeong, H., Yi, S. K., Kyeong, J., et al. 2013, *ApJS*, **208**, 7
- Jiang, P., Tang, N.-Y., Hou, L.-G., et al. 2020, *Research in Astronomy and Astrophysics*, **20**, 064
- Jing, W. C., Han, J. L., Hong, T., et al. 2023, *MNRAS*, **523**, 4949
- Kaneko, H., Kuno, N., Iono, D., et al. 2017, *PASJ*, **69**, 66
- Kim, D. C., Sanders, D. B., Veilleux, S., et al. 1995, *ApJS*, **98**, 129
- Maccagni, F. M., Morganti, R., Oosterloo, T. A., et al. 2017, *A&A*, **604**, A43
- Maccagni, F. M., Morganti, R., Oosterloo, T. A., & Mahony, E. K. 2014, *A&A*, **571**, A67
- Moreno, J., Torrey, P., Ellison, S. L., et al. 2019, *MNRAS*, **485**, 1320
- Morganti, R., Fogasy, J., Paragi, Z., et al. 2013, *Science*, **341**, 1082
- Morganti, R., Holt, J., Tadhunter, C., et al. 2011, *A&A*, **535**, A97
- Morganti, R., & Oosterloo, T. 2018, *A&A Rv*, **26**, 4
- Morganti, R., Oosterloo, T., Struve, C., & Saripalli, L. 2008, *A&A*, **485**, L5
- Morganti, R., Oosterloo, T. A., Tadhunter, C. N., et al. 2001, *MNRAS*, **323**, 331
- Morganti, R., Peck, A. B., Oosterloo, T. A., et al. 2009, *A&A*, **505**, 559
- Murthy, S., Morganti, R., Oosterloo, T., & Maccagni, F. M. 2021, *A&A*, **654**, A94
- Nan, R. 2006, *Science in China: Physics, Mechanics and Astronomy*, **49**, 129
- Nan, R., Li, D., Jin, C., et al. 2011, *International Journal of Modern Physics D*, **20**, 989
- Newville, M., Stensitzki, T., Allen, D. B., & Ingargiola, A. 2014, LMFIT: Non-Linear Least-Square Minimization and Curve-Fitting for Python, 0.8.0, Zenodo
- Oosterloo, T., Morganti, R., Crocker, A., et al. 2010, *MNRAS*, **409**, 500
- Peck, A. B., & Taylor, G. B. 2001, *ApJL*, **554**, L147
- Salim, S., Lee, J. C., Janowiecki, S., et al. 2016, *ApJS*, **227**, 2
- Schulz, R., Morganti, R., Nyland, K., et al. 2021, *A&A*, **647**, A63
- Serra, P., Oosterloo, T., Morganti, R., et al. 2012, *MNRAS*, **422**, 1835
- Srianand, R., Gupta, N., Momjian, E., & Vivek, M. 2015, *MNRAS*, **451**, 917
- Stark, D. V., Masters, K. L., Avila-Reese, V., et al. 2021, *arXiv*, [arXiv:2101.12680](https://arxiv.org/abs/2101.12680)
- Struve, C., & Conway, J. E. 2010, *A&A*, **513**, A10
- . 2012, *A&A*, **546**, A22
- Struve, C., Oosterloo, T. A., Morganti, R., & Saripalli, L. 2010, *A&A*, **515**, A67
- Toba, Y., Oyabu, S., Matsuhara, H., et al. 2014, *ApJ*, **788**, 45
- Tremblay, G. R., Oonk, J. B. R., Combes, F., et al. 2016, *Nature*, **534**, 218
- van Gorkom, J. H., Knapp, G. R., Ekers, R. D., et al. 1989, *AJ*, **97**, 708
- Virtanen, P., Gommers, R., Oliphant, T. E., et al. 2020, *NatMe*, **17**, 261
- Xu, C. K., Cheng, C., Appleton, P. N., et al. 2022, *Nature*, **610**, 461
- Yu, Q., Fang, T., Feng, S., et al. 2022, *ApJ*, **934**, 114
- Zhang, B., Zhu, M., Wu, Z.-Z., et al. 2021, *MNRAS*, **503**, 5385
- Zhu, M., Yu, H., Wang, J., et al. 2021, *ApJL*, **922**, L21

Table A1. H I Absorption Non-detections

Source name	R.A.	Decl.	t_{ON}	z	$S_{1.4 \text{ GHz}}$	$\log(P_{1.4 \text{ GHz}})$	rms	τ_{peak}	Radio type
	deg.	deg.	(min)		(mJy)	(W Hz ⁻¹)	(mJy)		
(1)	(2)	(3)	(4)	(5)	(6)	(7)	(8)	(9)	(10)
J0312-0004	48.01039	-0.07847	12.3	0.03762	14.7	22.68	0.19	<0.040	E
J0322-0000	50.63664	-0.00121	12.3	0.02175	17.2	22.27	0.18	<0.032	E
J0352-0620	58.05244	-6.34894	10.7	0.03295	12.5	22.50	0.22	<0.044	E
J0406-0506	61.68081	-5.11472	12.3	0.06600	14.2	23.18	0.21	<0.045	E
J0735+4212	113.98199	42.20336	12.3	0.08822	18.5	23.56	0.20	<0.033	C
J0746+3029	116.63530	30.49075	12.3	0.05704	16.3	23.10	0.20	<0.038	E
J0839+2308	129.96150	23.14335	21.3	0.02520	12.3	22.25	0.15	<0.037	C
J0850+5522	132.59502	55.37874	5.0	0.03076	20.0	22.64	0.30	<0.046	E
J0903+4026	135.75897	40.43399	12.3	0.02877	15.5	22.47	0.18	<0.029	C
J0920+0102	140.00904	1.03830	21.3	0.01703	10.7	21.84	0.17	<0.052	E
J1022+3634	155.58076	36.58304	5.3	0.02592	13.4	22.31	0.24	<0.055	E
J1106+4602	166.65570	46.03878	6.2	0.02501	16.3	22.37	0.23	<0.043	E
J1120+5049	170.16647	50.82729	5.0	0.02762	24.8	22.64	0.40	<0.050	E
J1124+4708	171.24463	47.14351	6.2	0.05372	10.5	22.86	0.23	<0.068	C
J1140+4632	175.19730	46.54049	12.3	0.05359	14.9	23.01	0.18	<0.037	E
J1153+5241	178.37742	52.68945	2.5	0.07164	23.0	23.46	0.45	<0.060	E
J1340+2629	205.23577	26.48672	5.0	0.07502	26.0	23.55	0.25	<0.029	C
J1423+4015	215.96472	40.25883	21.3	0.08220	12.1	23.31	0.15	<0.038	E
J1445+5134	221.43798	51.58082	16.0	0.02963	11.5	22.37	0.19	<0.051	C
J1539+4438	234.87364	44.64845	6.5	0.07299	20.6	23.43	0.32	<0.048	C
J1544+4330	236.21348	43.51406	21.3	0.03664	11.4	22.55	0.14	<0.038	E
J1624+2507	246.09814	25.13012	16.0	0.09603	12.6	23.47	0.21	<0.051	E
J2128+0017	322.04858	0.29988	21.3	0.05250	15.2	23.00	0.18	<0.036	E

Notes. The columns are (1) the source name of the AGN; (2) R.A. in degrees; (3) Decl. in degrees; (4) integration time; (5) redshift from SDSS spectroscopy (Abolfathi et al. 2018); (6) radio continuum flux at 1.4 GHz from NVSS (Condon et al. 1998); (7) radio power at 1.4 GHz; (8) 1σ noise measured at the velocity resolution of 16 km s⁻¹; (9) upper limit of the peak optical depth estimated with 3σ rms; (10) radio morphology classification as compact (C) and extended (E).